

Modified Rotor Flux Estimated Direct Torque Control for Double Fed Induction Generator

Mihir Mehta*[‡] , Dr. Bhinal Mehta** 

*M & V Patel Department of Electrical Engineering, CSPIT, Charotar University of Science and Technology, CHARUSAT Campus, Changa, Gujarat 388421, India

**Electrical Engineering Department, School of Technology, Pandit Deendayal Energy University, Gandhinagar, Gujarat, India

(mihirmehta.ee@charusat.ac.in, bhinal.mehta@sot.pdpu.ac.in)

[‡]Corresponding Author; Mihir Mehta, Charotar University of Science and Technology, CHARUSAT Campus, Changa 388421, Gujarat, India, Tel: +91 7405856957,

mihirmehta.ee@charusat.ac.in

Received: 02.12.2021 Accepted: 11.01.2022

Abstract- The paper deals with an essential approach, Direct Torque Control (DTC) that can control the torque of induction machine-based wind turbine generating systems. As the penetration of renewable energy sources is increasing abundantly, various system operators are implementing stringent grid codes globally. Power quality and harmonics are some of the most important grid codes and the proposed control aims to help in the area by providing a decoupled control of torque and flux. The main disadvantage of conventional DTC is high torque and flux ripples. The paper contends a DTC control scheme using fractional order PID controller (FPID) implemented on double-fed induction machine (DFIM) based wind turbine generating systems. Proposed control logic conjectures rotor flux and electromagnetic torque based on rotor voltage, current, and speed measurements as inputs. This paper unfurls the results validated using MATLAB Simulink for active and reactive power, DC link voltage, line current, and electromagnetic torque.

Keywords Active Power Control, DFIG, DTC, FPID, Reactive Power Control

1. Introduction

Wind and solar energy are two of the most common renewable energy sources on the planet [1-2], not only because of their clean availability and environmental friendliness, but also because of their cost-effectiveness. A contemporary wind parks' (WP) first choice is variable-speed wind turbines (WTs). The main reasons for achieving this objective are, first and foremost, maximum wind energy absorption, second, compliance with grid code requirements, third, reduction of drive train stresses [3], and many other essentials for grid integration [4]. Wind parks with doubly fed induction machines (DFIM) are one of the most sought-after configurations in recent years [5], because they can provide decoupled control of both active and reactive power. Moreover, inverter costs are also decreased, and the system can operate over a wide variety of wind speeds. Furthermore, literature dealing with various control techniques and algorithms applied to doubly-fed induction generators (DFIG)

has been studied [6-22] to build an efficient grid-linked Wind Energy Conversion System (WECS).

Direct torque control was later developed for DFIG [6-8]. The fundamental block diagram in Figure 1 depicts the traditional direct torque control (DTC) applied to DFIG. DTC chooses a suitable voltage vector using an appropriate switching table to limit the errors of the flux and torque in their resulting hysteresis band. DTC offers an advantage over stator flux orientation because it has qualities such as rapid dynamic reaction, simple construction, and low dependence on machine factors [9]. As a result, DTC has been a major focus of study across the world. The author of this paper aimed to improve the dynamic performance of traditional DTC by enhancing the line currents, DC link voltage, electromagnetic torque, active power, and reactive power at the point of common coupling.

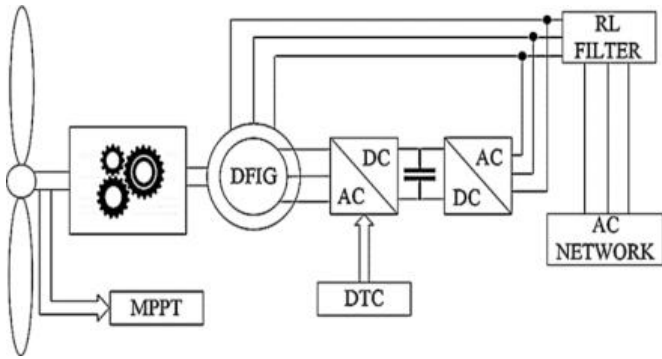


Fig. 1. Block Diagram – Conventional DTC algorithm applied to DFIG.

Other suggested DTC systems use various vectors to eliminate errors from both flux and torque by using zero vector first and then active vector from traditional DTC. Various concepts have been utilized, including mean torque equalization in comparison to the reference torque with each cycle [10-11], calculating the duty ratio of the zero vectors and active vectors for reducing torque ripples [12-13], fuzzy logic implementation [14-16], fault-ride-through (FRT) [17-19], use of matrix converter [20] and the use of optimization algorithms and hybrid controllers [21-22]. The author proposes a method that uses a modified filter to decrease torque and flux ripples. Furthermore, instead of hysteresis bands, fractional-order self-tuning PID controllers are used to regulate the DQ-axis voltages fed to the machine-side converter.

At the very outset, the author would like to declare the scheme of the research paper that engages with mathematical modelling of DFIG wind turbine, conventional flux estimation topology, conventional control strategy, proposed flux estimation topology, proposed control strategy, test system, and simulation results followed by the conclusion.

2. Mathematical Modelling of DFIG Wind Turbine

The power of the wind crossing the blades of the wind turbine is in the form of kinetic energy and can be represented as shown in Eq. (1)

$$P_v = \frac{1}{2} \rho A_1 V_v^3 \tag{1}$$

Where, ρ = Air Density, A_1 = Surface area, V_v = Wind Speed.

Unfortunately, the turbine can recuperate only a part of this power as explained in Eq. (2)

$$P_t = \frac{1}{2} \rho \pi R^2 V_v^3 C_p \tag{2}$$

Where, R = Radius of the wind turbine; C_p = Co-efficient of Power.

The mechanical torque can be calculated using Eq. (3)

$$T_m = \frac{P_m}{\omega_r} \tag{3}$$

Where ω_r = Mechanical Angular Speed

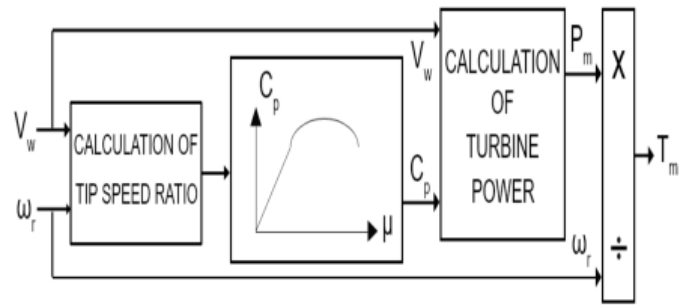


Fig. 2. Wind Turbine Model

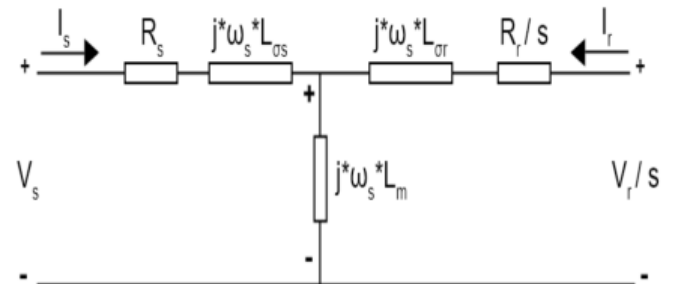


Fig. 3. Single-phase steady-state equivalent circuit of DFIG referred to stator

Figure 2 represents the wind turbine model and Figure 3 reflects the single-phase steady-state equivalent circuit of DFIG referred to stator. Dynamic mathematical modelling of DFIM as a generator under a synchronously rotating d-q reference frame necessitates the voltage equations as shown in Eq. (4-7).

$$V_{ds} = R_s I_{ds} + \frac{d}{dt} \Psi_{ds} - \omega_s \Psi_{qs} \tag{4}$$

$$V_{qs} = R_s I_{qs} + \frac{d}{dt} \Psi_{qs} - \omega_s \Psi_{ds} \tag{5}$$

$$V_{dr} = R_s I_{dr} + \frac{d}{dt} \Psi_{dr} - (\omega_s - \omega_r) \Psi_{qr} \tag{6}$$

$$V_{qr} = R_s I_{qr} + \frac{d}{dt} \Psi_{qr} + (\omega_s - \omega_r) \Psi_{dr} \tag{7}$$

Here, V_{qs} , I_{ds} , I_{qs} , Ψ_{ds} and Ψ_{qs} are the stator voltages, current, and flux in d-axis and q-axis respectively, whereas, V_{qr} , I_{dr} , I_{qr} , Ψ_{dr} and Ψ_{qr} the rotor voltage, current, and flux in d-axis and q-axis respectively. R_s is the stator resistance, while ω_s and ω_r are the stator and rotor angular velocities respectively.

The expression of stator and rotor fluxes can be expressed as shown in Eq. (8-11)

$$\Psi_{ds} = L_s I_{ds} + L_m I_{dr} \tag{8}$$

$$\Psi_{qs} = L_s I_{qs} + L_m I_{qr} \tag{9}$$

$$\Psi_{dr} = L_r I_{dr} + L_m I_{ds} \tag{10}$$

$$\Psi_{qr} = L_r I_{qr} + L_m I_{qs} \tag{11}$$

Where, L_s , L_r and L_m are the stator inductance, rotor inductance, and mutual inductance respectively. The

electromagnetic torque T_{em} is expressed as shown in Eq. (12) where, $I_{r\alpha}$, $I_{r\beta}$, $\psi_{r\alpha}$ and $\psi_{r\beta}$ are the rotor current and rotor flux in α and β reference frame respectively and p is the number of pole pairs.

$$T_{em} = \frac{3}{2} p(I_{r\beta}\psi_{r\alpha} - I_{r\alpha}\psi_{r\beta}) \quad (12)$$

The equivalent circuit of d-q model of DFIG as shown in Figure 4.

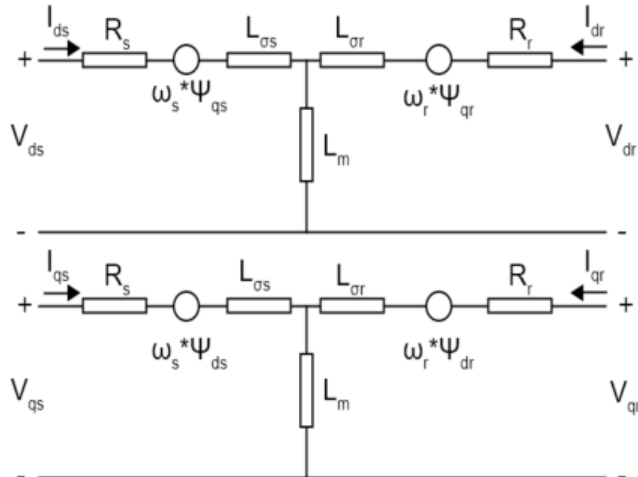


Fig. 4. D-Q axis equivalent model of DFIG

3. Conventional Flux Estimation Topology

The expression of rotor flux derived from rotor voltage of DFIG in $\alpha\beta$ reference frame is as stated in Eq. (13-14) –

$$\left\{ \begin{aligned} V_{r\alpha} &= R_r I_{r\alpha} + \frac{d\psi_{r\alpha}}{dt} \\ \Rightarrow \psi_{r\alpha} &= \int (V_{r\alpha} - R_r I_{r\alpha}) dt \end{aligned} \right\} \quad (13)$$

$$\left\{ \begin{aligned} V_{r\beta} &= R_r I_{r\beta} + \frac{d\psi_{r\beta}}{dt} \\ \Rightarrow \psi_{r\beta} &= \int (V_{r\beta} - R_r I_{r\beta}) dt \end{aligned} \right\} \quad (14)$$

Where, $V_{r\alpha}$, $V_{r\beta}$ are the rotor voltage and R_r is the rotor resistance.

4. Conventional Control Strategy

The block diagram of conventional DTC control scheme, on the DFIG wind turbine generating system is as shown in the Figure 5, which contains multiple blocks namely rotor-side converter (RSC) which is connected to the rotor of DFIG, grid-side converter (GSC) which is connects the stator of DFIG to grid.

Various signals like the voltage, current, and speed of the rotor are received from the machine, which are further used for computing the rotor flux and electromagnetic torque. These electromagnetic torque and rotor flux signals are compared with the reference which results in deviations. These deviations generated are being consumed by the hysteresis controllers. The rotor flux hysteresis ON-OFF controller is a 2-stage comparator whereas the electromagnetic

torque hysteresis ON-OFF controller is a 3-stage comparator and can be noticed in Figure 6.

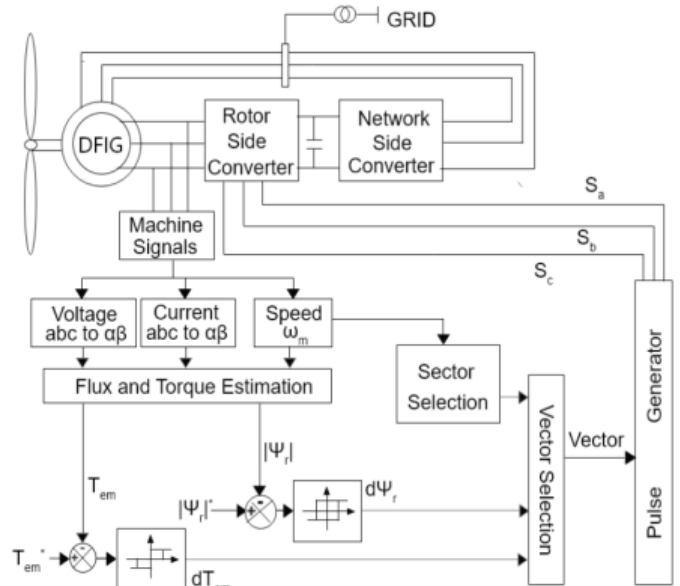


Fig. 5. Conventional DTC Control Scheme

The output received from the hysteresis controllers are $d\psi_r$ and dT_{em} . The value of $d\psi_r$ can be 1 or -1, while the value of dT_{em} can be 1, 0 or -1. To improve the accuracy and to mitigate the ripples in the required torque and flux signals, the flux hysteresis ON-OFF controller is set to 1.5% of the rated flux while the torque hysteresis band is set to 5% of the rated torque.

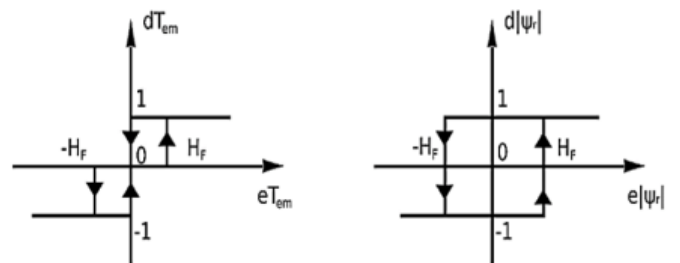


Fig. 6. Hysteresis Comparators

Apart from estimating the magnitude of the rotor flux in the $\alpha\beta$ reference frame, it is also equally important to locate the position of rotor flux vector i.e. the rotor flux angle. Based on this information, the sector selection is accomplished as per look-up table shown in Table 1.

Table 1. Sector Selection Look-Up Table

Rotor Flux Angle Range		Selected Sector
0^0	30^0	1
$> 30^0$	90^0	2
$> 90^0$	150^0	3
$> 150^0$	210^0	4
$> 210^0$	270^0	5
$> 270^0$	330^0	6
$> 330^0$	0^0	1

The combination of the sector having rotor flux vector and the received output of hysteresis controller allow the voltage selector block to select an appropriate voltage vector for the pulse generator block as represented in Figure 5. The selected voltage vectors can be further subdivided into two categories – Active Vectors and Inactive vectors. Only when the value of $d\psi_r = 0$ an inactive voltage vector is selected. In the rest of the cases, an active voltage vector is adopted.

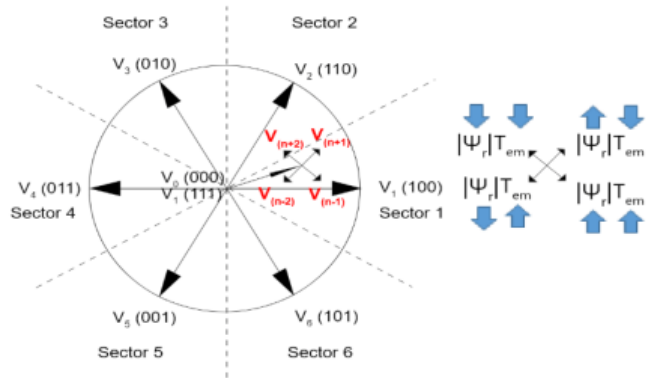


Fig. 7. Effect of Voltage Vectors on Rotor Flux and Electromagnetic Torque amplitude

The selected voltage vector corrects the torque and the flux errors as shown in Figure 7, where n represents the sector number. Later the pulse generator generates the pulses for the semiconductor switches of the 2-level converter. Table 2, pulse generation look-up, defines the determination of a particular pulse due to the presence of a particular vector in a pulse generator.

Table 2. Pulse Generator Look-Up Table

Selected Voltage Vector	S_a	S_b	S_c
V_7	1	1	1
V_6	1	0	1
V_5	0	0	1
V_4	0	1	1
V_3	0	1	0
V_2	1	1	0
V_1	1	0	0
V_0	0	0	0

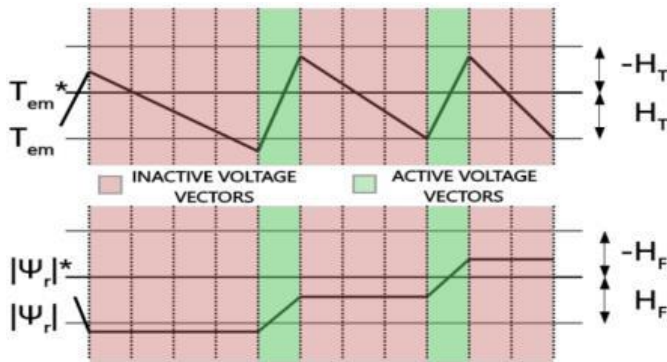


Fig. 8. Voltage Vectors and its Effect on Rotor Flux and Electromagnetic Torque

It is to be noted that the selected voltage vector does affect the electromagnetic torque as well as the rotor flux as shown in Figure 8. The selected voltage vector plays a vital role in the correction of deviations in the rotor flux as well as electromagnetic torque.

5. Proposed Flux Estimation Topology

It has been observed that in the practical application the pure inductor is manipulated by the error in the initial value and DC drift. To overcome this issue author suggests using a modified filter over pure integrator as shown in Figure 9 and its transfer function is as follows. The modified filter has a cut-off frequency which is represented by ω_f while the operating frequency of DFIG by ω . The DFIG is connected to a grid of 60 Hz and a filter is tuned as 10Hz, the angular frequency are –

$$\omega = 2\pi * 60 = 376.99 \text{ rad / s} \tag{15}$$

$$\omega_f = 2\pi * 10 = 62.83 \text{ rad / s} \tag{16}$$

Transfer function can be represented as shown in Eq. (17) –

$$G(s) = \frac{1}{s + \omega_f} = \frac{s}{s + \omega_f} \frac{1}{s} \tag{17}$$

Thus the generated error is –

$$\epsilon_{\text{mod}} = \sqrt{1 + \frac{\omega_f^2}{\omega^2}} \tag{18}$$

$$\epsilon_{\text{ang}} = -90 + a \tan \frac{\omega}{\omega_f} \tag{19}$$

Hence, the estimated flux linkages are derived as –

$$\left\{ \begin{aligned} \psi_{r\alpha}'(s) &= \psi_{r\alpha}(s) \frac{s}{s + \omega_f} \\ \Rightarrow \psi_{r\alpha}(s) &= \psi_{r\alpha}'(s) + \psi_{r\alpha}'(s) \frac{\omega_f}{s} \end{aligned} \right\} \tag{20}$$

$$\left\{ \begin{aligned} \psi_{r\beta}'(s) &= \psi_{r\beta}(s) \frac{s}{s + \omega_f} \\ \Rightarrow \psi_{r\beta}(s) &= \psi_{r\beta}'(s) + \psi_{r\beta}'(s) \frac{\omega_f}{s} \end{aligned} \right\} \tag{21}$$

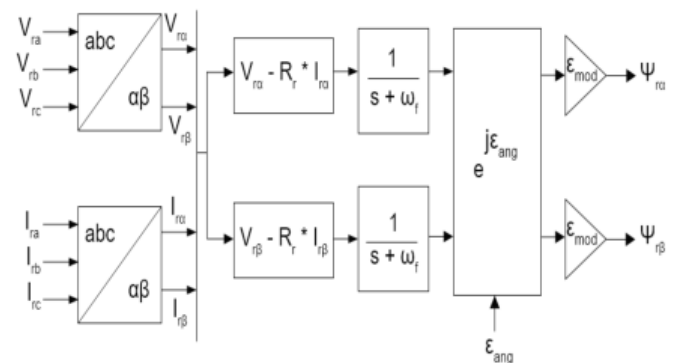


Fig. 9. Proposed Flux Control Logic

6. Proposed Control Logic

The facet of proposed torque control method are quick dynamic response, easy execution in circuit and demands fewer alterations in the existing design. The author here adopts dq-reference frame to explain the concept. Since the value of stator resistance is comparatively very small, the equation of the modified stator flux can be as mentioned below –

$$\Psi_{sd} = \Psi_s \tag{22}$$

$$\Psi_{sq} = 0 \tag{23}$$

Similarly, the modified stator voltages can be represented as –

$$V_{sd} = 0 \tag{24}$$

$$V_{sq} = \omega_s \Psi_s \tag{25}$$

The modified stator currents in dq reference frame can also be represented as –

$$I_{sd} = \frac{\Psi_{sd} - L_m I_{rd}}{L_s} \tag{26}$$

$$I_{sq} = \frac{L_m I_{rq}}{L_s} \tag{27}$$

The modified rotor fluxes in dq reference frame are represented as –

$$\Psi_{rd} = L_r \sigma I_{rd} + \frac{L_m}{L_r} \Psi_{sd} \tag{28}$$

$$\Psi_{rq} = L_r \sigma I_{rq} \tag{29}$$

Here σ is the dispersion coefficient and it can be represented as –

$$\sigma = 1 - \frac{L_m^2}{L_s L_r} \tag{30}$$

The modified rotor voltages can be represented as –

$$V_{rd} = R_r I_{rd} - s \omega_s L_r \sigma I_{rq} \tag{31}$$

$$V_{rq} = R_r I_{rq} + s \omega_s L_r \sigma I_{rd} + s \frac{L_m}{L_s} V_{sq} \tag{32}$$

The above two equations explains the relationship between the rotor voltages and the rotor currents. Hence the modified and decoupled control of active as well as reactive power of stator can be achieved by using dq axis components of rotor current as represented below –

$$P_s = 1.5 V_{sq} I_{sq} = -1.5 \frac{L_m}{L_s} V_{sq} I_{rq} \tag{33}$$

$$Q_s = 1.5 V_{sq} I_{sd} = 1.5 V_{sq} \left[\frac{V_{sq}}{L_s \omega_s} - \frac{L_m}{L_s} I_{rd} \right] \tag{34}$$

In the proposed control strategy, the deviations of electromagnetic torque and rotor flux are smaller compared to the deviations of the conventional control method as the actuating quantities are forced to pass through the modified filter as shown in Figure 10. These deviations are being consumed by fractional order proportional, integral and derivative controller (FPID).

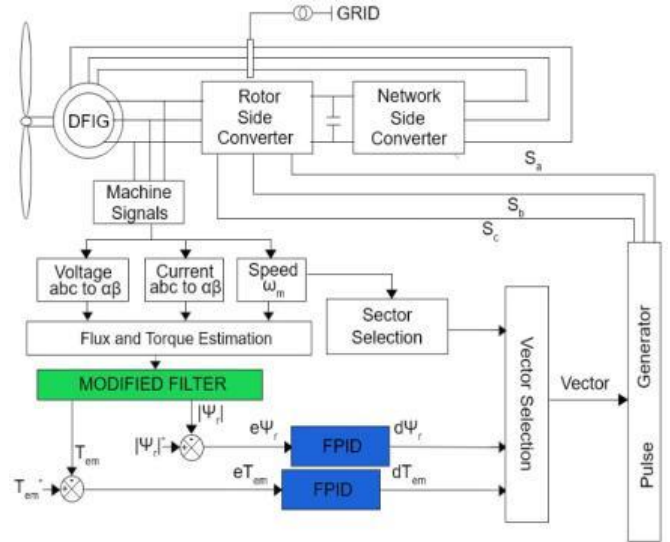


Fig. 10. Control Strategy Diagram of the Proposed Topology

The differential equation used to reduce the deviation of the rotor flux using FPID controller is given by –

$$d\Psi_r(t) = k_p e\Psi_r(t) + k_i D_t^{-\lambda} e\Psi_r(t) + k_d D_t^\mu e\Psi_r(t) \tag{35}$$

Similarly, the differential equation used to reduce the deviation of the rotor flux using FPID controlled is given by –

$$dT_{em}(t) = k_p eT_{em}(t) + k_i D_t^{-\lambda} eT_{em}(t) + k_d D_t^\mu eT_{em}(t) \tag{36}$$

The parameters FPID controller are tuned with the help of FPID Optimization tool in MATLAB. The objective function is considered by adding the time weightage to the integral absolute error (IAE) and becomes integral time absolute error (ITAE).

$$ITAE = \int_0^t t (|\Delta T_{em}| + |\Delta \Psi_r| + |\Delta I|) \tag{37}$$

Value of k_p , k_i and k_d can be tuned initially, keeping the values of λ and μ as 1. Thereafter, a proper range for the gains and their exponentials are decided within which FPID will try to provide the most optimized results. Table 3 provides the information on the initial values utilized with parameter constrain range.

Table 3. Controller parameter values and its range

Parameter	Values		
	Initial	Minimum	Maximum
k_p	19.20	0	100
k_i	3.9	0	50
k_d	2.97	0	50
λ	1	0.001	1
μ	1	0.001	1

The optimization function provides heavy penalizing of late occurring deviations whereas deviations in the initial stages get a minimal weightage. The performance of the FPID

block is optimized by using the following flow chart shown in Fig. 11.

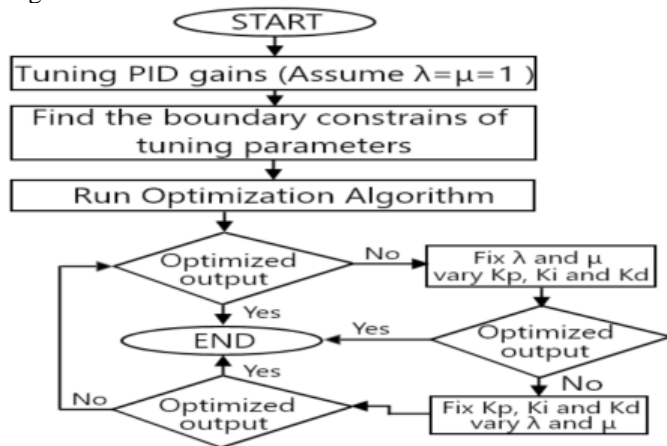


Fig. 11. FPID Optimization Flow Chart

To get the best outcomes, the optimization method seeks to fix the value of λ and μ , while changing the values of k_p , k_i and k_d . The procedure is discontinued after the optimal outcomes have been attained. If, on the other hand, the optimal outcomes are not obtained, the gains k_p , k_i and k_d are maintained fixed while the values of λ and μ are changed. This method is repeated until an optimal outcome is obtained.

The voltage selector block receives these optimized outputs together with information about the sector in which the vector is presently situated. This would aid in the selection of the most optimal voltage vectors to supply to the pulse generators, allowing the pulses to be sent to the DFIG machine side converter. One can observe how the system's performance has improved in the discussion part of the simulation results.

7. Test System

Figure 12 represents the test system consisting of six DFIG-WT of 1.5MW each comprising of a 9MW wind farm operating at unity power factor. The WTs are connected to a 25KV distribution system which transfers power to a 120KV grid. A 30-kilometer feeder of 25KV can be seen between PCC and bus B1, which connects to the grid.

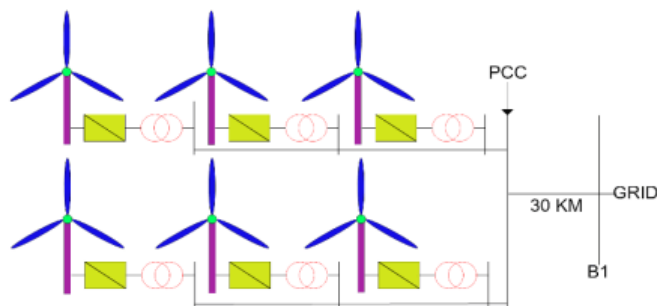


Fig. 12. Test System

8. Results and Discussion

This section contains a comparison of the traditional and suggested control strategies, with the proposed scheme showing a substantially superior and improved dynamic

behavioural response of DFIG. The system experiences a failure in which the voltage variation drops to 50% of its original value at 1.5 seconds and then restored to its original value at 2.0 seconds. The standard control method and the suggested control technique's positive and negative peaks are compared, and the peak magnitudes are reduced as a result.

Figure 13 represents the per unit line current at bus B1 at the commencement of the fault. The positive peak appeared 1.503 seconds, whereas the negative peak appeared 1.506 seconds after the commencement of the fault. The magnitudes of the positive and negative peaks in the traditional system are 1.595 and -1.51, respectively, however they are 1.426 and -1.348 in the proposed system. The diminution in the positive as well as negative peaks are 10.59 and 10.72 percent, respectively.

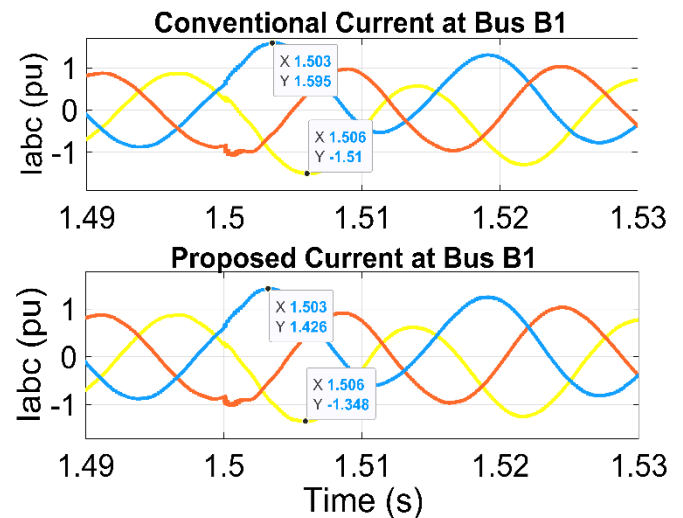


Fig. 13. Comparison of line currents at bus B1 at the commencement of the fault

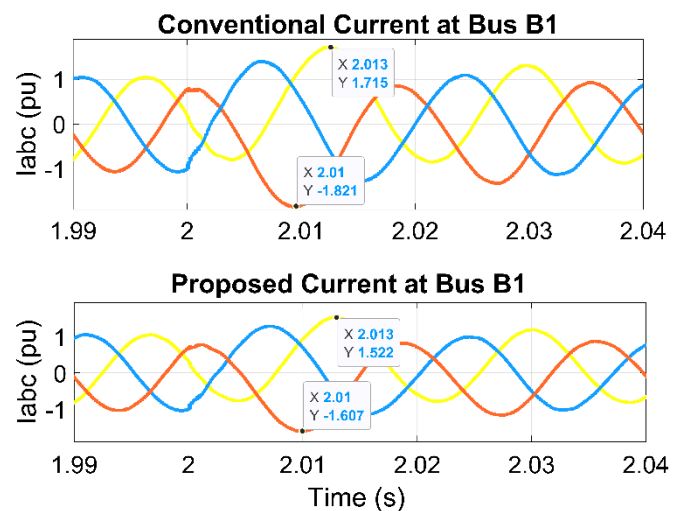


Fig. 14. Comparison of line currents at bus B1 on clearing of the fault

The per unit line current at bus B1 at the end of the fault is shown in the Figure 14. When the fault has been fixed the positive peak occurred at 2.013 seconds, whereas the negative peak appeared at 2.01 seconds. In the existing scheme, the positive and negative peaks have magnitudes of 1.715 and -1.821, respectively, whereas in the proposed system, they

possess magnitudes of 1.522 and -1.607. The positive and negative peaks have shrunk by 11.25 percent and 11.75 percent, respectively.

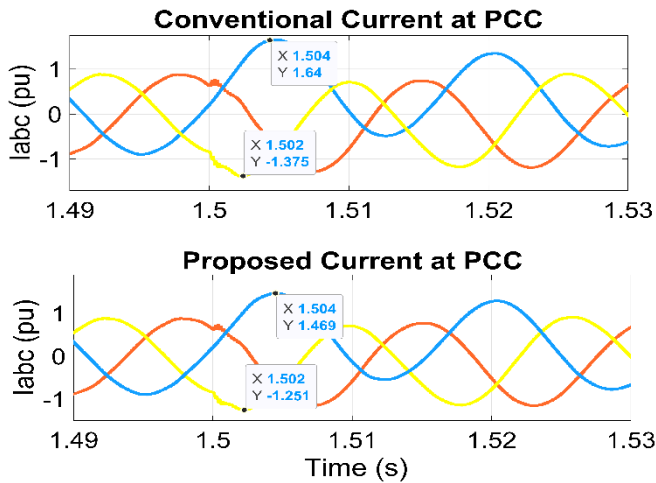


Fig. 15. Comparison of line currents at PCC at the commencement of the fault

The per unit line current at PCC at the commencement of the fault is depicted in the Figure 15. In the traditional system, the value of positive peak at instance 1.504 second is 1.64 pu, but in the suggested method, the peak reached is 1.469 pu, yielding an overall reduction of 10.42 percent. Furthermore, the traditional system detects a negative peak of -1.375 pu at 1.502 seconds, but the suggested system detects a negative peak of -1.251 pu at the same time, decreasing the magnitude by 9.018 percent.

Figure 16 represents the per unit line current at the completion of the fault at PCC. The positive peaks are measured at 2.008 seconds whereas the negative peaks are measured at 2.011 seconds. The positive peak has a value of 1.694, whereas the negative peak has a value of -1.835 using the conventional topology. The proposed topology, on the other hand, has values of 1.508 during the positive peak and -1.613 at the negative peak. As a result, there is a noticeable drop in both the positive peak of 10.98 percent and the negative peak of 12.09 percent in the proposed topology.

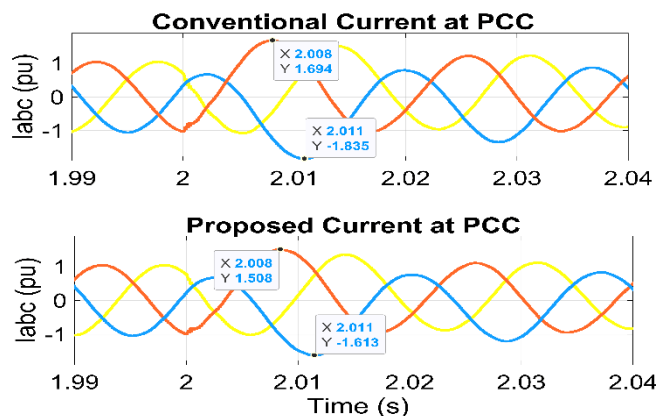


Fig. 16. Comparison of line currents at PCC on clearance of the fault

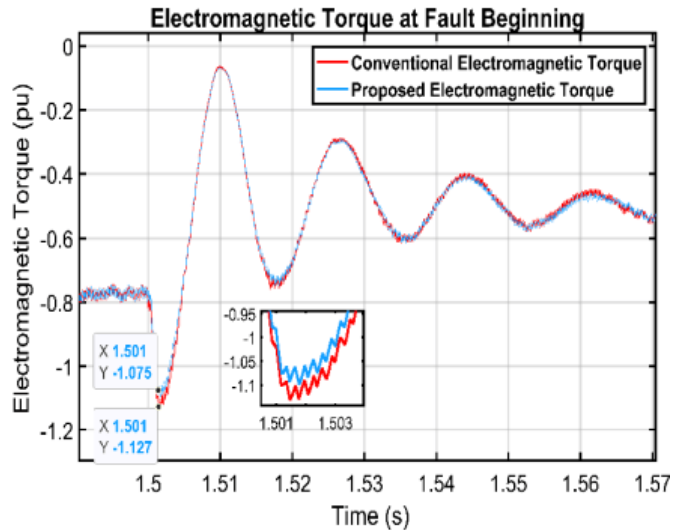


Fig. 17. Electromagnetic torque at the commencement of the fault

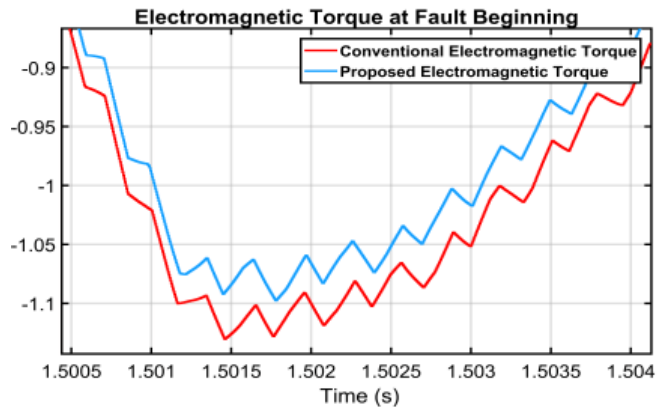


Fig. 18. Magnified deviation in electromagnetic torque after the commencement of fault

Figure 17 illustrates the comparisons of the first peak at 1.501 seconds after the fault commencement. The peak values for the conventional and suggested systems are -1.127 p.u. and -1.075 p.u., respectively, indicating a 4.66 percent reduction in the peak value. Figure 18 represents the deviation in the peak generated by the conventional topology and proposed topology, right after the commencement of the fault.

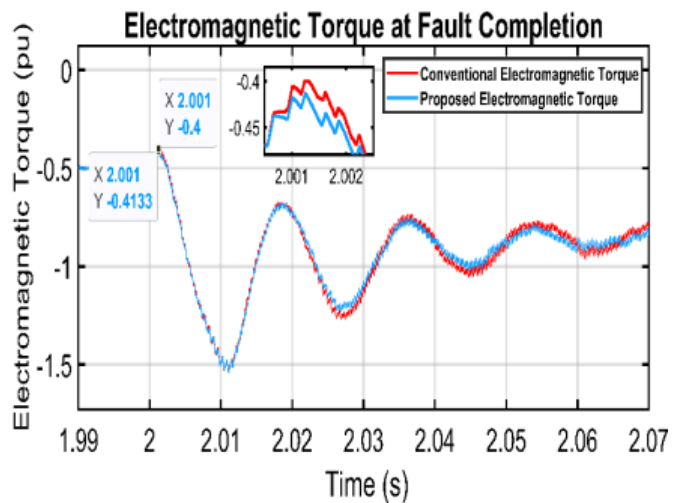


Fig. 19. Electromagnetic torque at the clearance of the fault

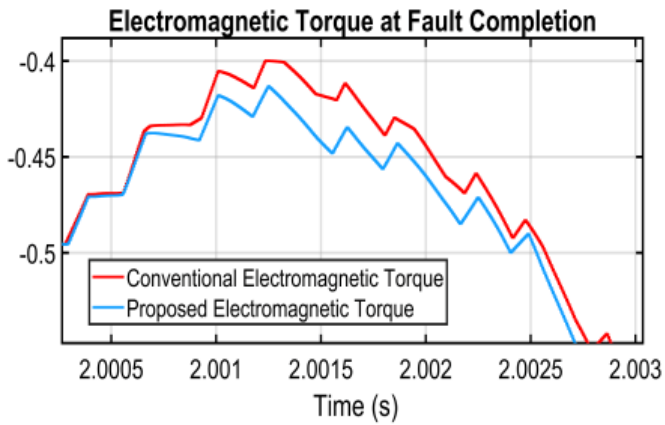


Fig. 20. Magnified deviation in electromagnetic torque on clearance of fault

Figure 19 shows the comparative findings of the first peak generated by both the systems, at time 2.001 seconds, after fault clearing. The conventional system generates the peak of magnitude -0.4 p.u. while that of the suggested system generates the peak of -0.4133 p.u. In comparison to the traditional method, the suggested approach shows a peak reduction of roughly 2.22 percent. Figure 20 reflects the deviation in the peak generated by the conventional topology and proposed topology, right after the clearance of the fault.

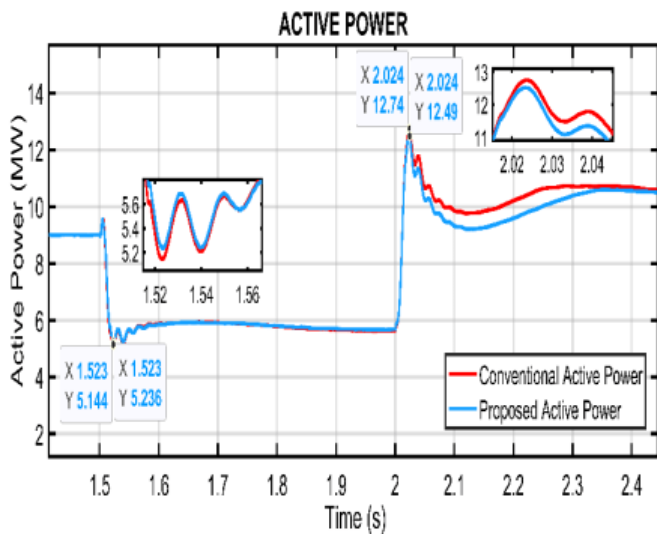


Fig. 21. Active power during the fault.

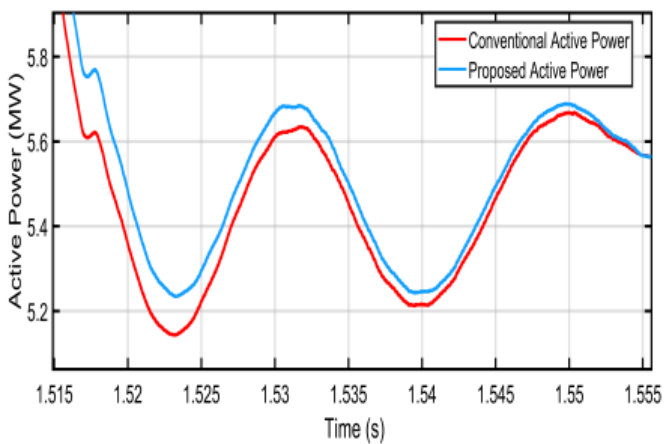


Fig. 22. Deviation in active power peak after the commencement of fault

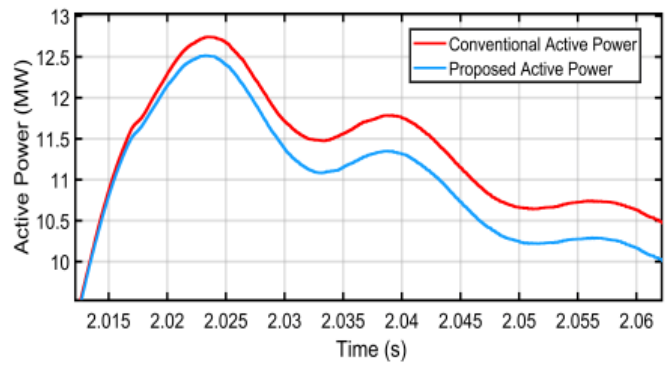


Fig. 23. Deviation in active power peak after the clearance of fault

The Figure 21 represents the active power comparison of the conventional and the proposed control topologies. The suggested control topology outperforms standard control topologies in terms of dynamic behaviour. Figure 22 reflects the first peak formed after the occurrence of the fault at 1.523 seconds indicates the active power of 5.144 MW in the conventional topology whereas in proposed topology it is 5.236 MW. This indicates the reduction of 1.76 percent in peaks generated by the proposed scheme in comparison to that of the conventional scheme. An overshoot in the active power is also observed after the clearance of the fault, as shown in Figure 23, creating the peak at 2.024 seconds. The magnitude of the active power in the conventional system is 12.74 MW while that of the proposed system is 12.49 MW which displays yet another reduction of 1.96 percent.

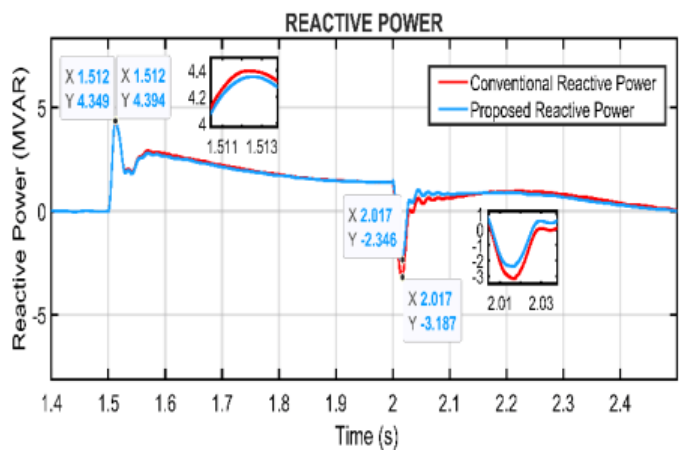


Fig. 24. Reactive power during the fault

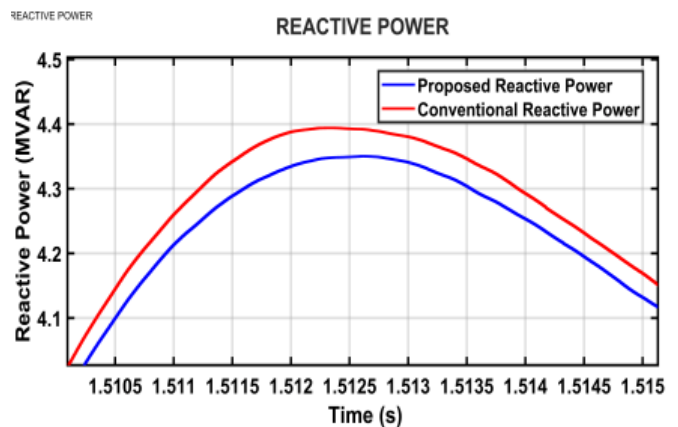


Fig. 25. Deviation in reactive power peak after the commencement of fault

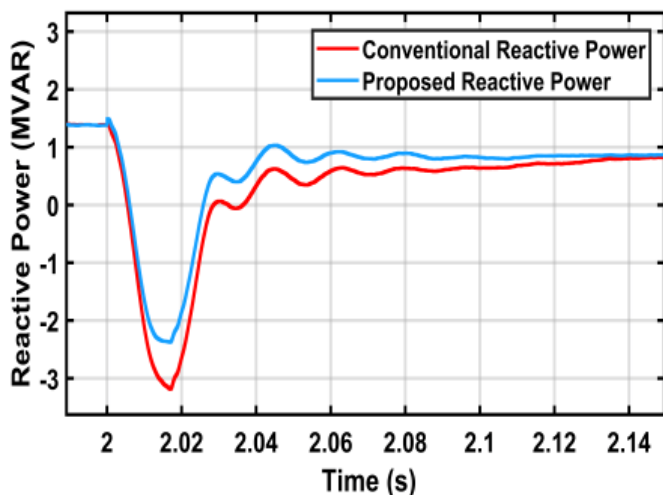


Fig. 26. Deviation in reactive power peak after the clearance of fault

Figure 24 depicts the comparison of the reactive power during the entire fault duration. Before the commencement of the fault, there is an overlap of the reactive power generated by the both the control schemes. The under voltage failure occurs after 1.5 second, resulting in a significant reactive power demand. Both topologies generate a positive peak at 1.512 seconds, although the peak generated by the traditional system is of the magnitude 4.394 MVAR and that of the proposed system is 4.349 MVAR. The magnified image of this deviation in the peaks is shown in the Figure 25, which displays the reduction in the peak by almost 1.02 percent. On the other hand, the fault is cleared at 2.0 seconds and a negative peak is formed by both the systems at 2.017 seconds. The magnitude generated by the conventional system is -3.187 MVAR while that of the proposed system is -2.346 MVAR. The magnified image of the same can be seen in Figure 26. Computation based on this data leads to a massive reduction in the lower peak by 26.39 percent generated by the proposed system.

The DC link voltages produced by the traditional topology and the suggested control method are compared in Figure 27. When the suggested technique is implemented, the fluctuation in DC link voltages is significantly minimized.

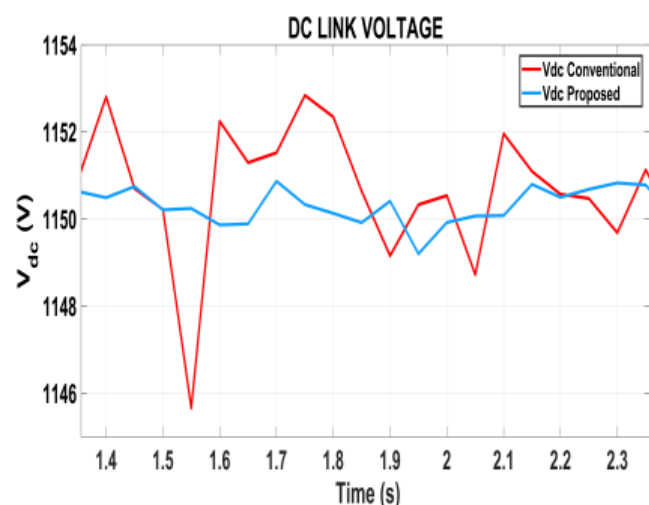


Fig. 27. DC link voltage during the voltage imbalance

9. Conclusion

This research reveals how the behaviour of a direct torque control method applied to DFIG may be improved during and after a fault occurs in terms of overshoot of line current, electromagnetic torque, active power, reactive power, and DC link voltage. This technique employs a modified filter and fractional order PID controllers to properly compute rotor flux and torque, which aids in the selection of the most appropriate voltage vectors and, ultimately, the firing of the DFIG's rotor side converter.

The positive peaks of the current at bus B1 and PCC have been reduced by at least 10.5 percent, while the negative peak has been reduced by at least 11.75 percent. 4.66 percent and 1.76 percent, respectively, are the minimal reductions in electromagnetic torque and active power. On the fault clearance, there is a substantial drop in reactive power peak of 26.39 percent. The findings were achieved with MATLAB Simulink, and they were determined to be superior to the traditional method.

References

- [1] G. Herbert, S. Iniyar, E. Sreevalsan, and S. Rajapandian, "A review of wind energy technologies", *Renewable and Sustain. Energy Reviews*, Vol. 11, No. 6, pp. 1117–1145, August 2007.
- [2] B. Sahu, "A study on global solar PV energy developments and policies with special focus on the top ten solar PV power producing countries", *Renewable and Sustain. Energy Reviews*, Vol. 43, pp. 621–634, March 2015.
- [3] A. Beainy, C. Maatouk, N. Moubayed, F. Kaddah, "Comparison of Different Types of Generator for Wind Energy Conversion System Topologies", 2016 3rd International Conference on Renewable Energies for Developing Countries, IEEE Press, pp. 1-6, July 2016.
- [4] B. Goud, and C. Reddy, "Essentials for grid integration of hybrid renewable energy systems: a brief review", *International Journal of Renewable Energy Research (IJRER)*, Vol. 10, No. 2, pp. 813-830, June 2020.
- [5] S. Saini, "Review of Doubly Fed Induction Generator Used in Wind Power Generation", *International Journal of Environmental Science: Development and Monitoring*, Vol. 4, No. 3, pp. 53–56, November 2013.
- [6] K. Gokhale, D. Karraker, and S. Heikkilä., Controller for Wound Rotor Slip Ring Induction Machine, U.S. Patent, 6,448,735 B1, September 10, 2002.
- [7] A. Kuroiwa, and K. Deguchi, Controller for Wound Rotor Slip Ring Induction Machine, U.S. Patent, 7,049,194 B1, May 9, 2006.
- [8] Y. Li, L. Hang, G. Li, Y. Guo, Y. Zou, J. Chen, J. Li, J. Zhuang, S. Li, "An improved DTC controller for DFIG-based wind generation system", 2016 IEEE 8th International Power Electronics and Motion Control Conference, Hefei, pp. 1423–1426, May 2016.

- [9] X. Garcia, B. Zigmund, A. Terlizzi, R. Pavlanin, and L. Salvatore, "Comparison between FOC and DTC Strategies for Permanent Magnet Synchronous Motors", *Advances in Electrical and Electronic Engineering*, Vol. 5, No. 1, pp. 76–81.
- [10] Y. Zhang, J. Zhu, W. Xu, and Y. Guo, "A simple method to reduce torque ripple in direct torque-controlled permanent-magnet synchronous motor by using vectors with variable amplitude and angle", *IEEE Trans on Ind. Electron.*, vol. 58, no. 7, pp. 2848–2859, July 2011.
- [11] K. Shyu, J. Lin, V. Pham, M. Yang, and T. Wang, "Global minimum torque ripple design for direct torque control of induction motor drives", *IEEE Trans. Ind. Electron.*, vol. 57, no. 9, pp. 3148–3156, September 2010.
- [12] J. Kang and S. Sul, "New direct torque control of induction motor for minimum torque ripple and constant switching frequency", *IEEE Trans Ind. Appl.*, vol. 35, no. 5, pp. 1076–1082, October 1999.
- [13] L. Tang, L. Zhong, M. Rahman, and Y. Hu, "A Novel Direct Torque Controlled Interior Permanent Magnet Synchronous Machine Drive With Low Ripple in Flux and Torque and Fixed Switching Frequency", *IEEE Trans Power Electron.*, vol. 19, no. 2, pp. 346–354, March 2004.
- [14] S. Gdaim, A. Mtibaa, and M. Mimouni, "Design and experimental implementation of DTC of an induction machine based on fuzzy logic control on FPGA", *IEEE Trans Fuzzy Syst.*, vol. 23, no. 3, pp. 644–655, June 2015.
- [15] A. Berzoy, J. Rengifo, and O. Mohammed, "Fuzzy Predictive DTC of Induction Machines with Reduced Torque Ripple and High-Performance Operation", *IEEE Trans. Power Electron.*, vol. 33, no. 3, pp. 2580–2587, March 2018.
- [16] F. Aymen, N. Mohamed, S. Chayma, C. Reddy, M. Alharthi, and S. Ghoneim, "An Improved Direct Torque Control Topology of a Double Stator Machine Using the Fuzzy Logic Controller". *IEEE Access*, Vol. 9, pp. 126400-126413.
- [17] L. Romeral, A. Arias, E. Aldabas, and M. Jayne, "Novel direct torque control (DTC) scheme with fuzzy adaptive torque-ripple reduction," *IEEE Trans. Ind. Electron.*, vol. 50, no. 3, pp. 487–492, June 2003.
- [18] L. Huchel, M. Moursi, and H. Zeineldin, "A Parallel Capacitor Control Strategy for Enhanced FRT Capability of DFIG", *IEEE Trans. Sustain. Energy*, vol. 6, no. 2, pp. 303–312, April 2015.
- [19] M. Elshiekh, D. Mansour, and A. Azmy, "Improving fault ride-through capability of DFIG - based wind turbines using superconducting fault current limiter", *IEEE Trans. Appl. Supercond.*, vol. 23, no. 3, pp. 1–5, June 2013.
- [20] X. Tian, W. Wang, X. Li, Y. Chi, Y. Li, H. Tang, "Fault ride through strategy of DFIG using rotor voltage direct compensation control under voltage phase angle jump", *CSEE Journal of Power Energy Systems*, Vol. 5, No. 4, pp. 515–523.
- [21] B. Goud, P. Varma, B. Rao, M. Reddy, A. Pandian, and C. Reddy, "Cuckoo Search Optimization based MPPT for Integrated DFIG-Wind Energy System", 2020 International Conference on Decision Aid Sciences and Application (DASA), Bahrain, pp. 636-639, 8-9 November 2020.
- [22] C. Reddy, K. Naresh, P. Reddy, and P. Sujatha, "Control of DFIG Based Wind Turbine with Hybrid Controllers", *International Journal of Renewable Energy Research (IJRER)*, Vol. 10, No. 3, pp. 1488-1500, September 2020.
- [23] M. Quraan, Q. Farhat and M. Bornat, "A new control scheme of back-to-back converter for wind energy technology", 2017 IEEE 6th International Conference on Renewable Energy Research and Applications, (ICRERA), San Diego, pp. 354-358, 5-8 November 2017.
- [24] Y. Elsayed, N. Saad and A. Zekry, "Assessing Wind Energy Conversion Systems Based on Newly Developed Wind Turbine Emulator", *International Journal of Smart Grid (ijSmartGrid)*, Vol. 4, No. 4, pp. 139-148, December 2020.
- [25] S. Abderrahim, M. Allouche and M. Chaabane, "A New Robust Control Strategy for a Wind Energy Conversion System Based on a T-S Fuzzy Model", *International Journal of Smart Grid (ijSmartGrid)*, Vol. 4, No. 2, pp. 88-99, June 2020.
- [26] F. Ayadi, I. Colak, I. Garip, and H. Bulbul, "Impacts of Renewable Energy Resources in Smart Grid.", 8th International Conference on Smart Grid (icSmartGrid), Paris, pp. 183-188, 17-19 June 2020.
- [27] H. Benbouhenni, "Stator Current and Rotor Flux Ripples Reduction of DTC DFIG Drive Using FSTSMC Algorithm", *International Journal of Smart Grid (ijSmartGrid)*, Vol. 3, No. 4, pp. 226-234, December 2019.